AIAA JOURNAL
Vol. 50, No. 12, December 2012

Large-Eddy Simulation of Jet in Supersonic Crossflow with Different Injectant Species

Junya Watanabe,* Toshinori Kouchi,† Kenichi Takita,‡ and Goro Masuya§
Tohoku University, Sendai 980-8579, Japan

DOI: 10.2514/1.J051550

The effects of injectant species on the turbulent structure and mixing state of jets in supersonic crossflow were investigated using a large-eddy simulation. Hydrogen, helium, nitrogen, and ethylene were transversely injected into a Mach 1.9 airflow at a constant jet-to-crossflow momentum flux ratio. The time-averaged distribution of jet concentration was roughly the same for all the injectant species, but the large-scale structure of scalar fluctuation differed significantly. The probability density functions of injectant mass fraction revealed that the turbulent behavior of nitrogen and ethylene jets was highly intermittent. The velocity field was considerably different between the injectants, owing to the different injection velocities. The hydrogen and helium jets had a much higher velocity difference between jet and crossflow in the near field; thus, the observed turbulent intensities for these two injectants were much higher than those for nitrogen and ethylene. In addition, the spectral analysis of velocity fluctuations in the windward mixing layer showed that the scale of energetic eddies was larger in the hydrogen and helium jets than in the nitrogen and ethylene jets. These characteristics resulted in better mixing in the hydrogen jet than in the ethylene jet for the studied injection conditions.

Nomenclature

C	=	molar concentration, mol/m^3
$c_{p,k}$	=	specific heat at constant pressure for species k, J/(kg · K)
D	=	injector diameter, m
D_k	=	diffusion coefficient for species k, m^2/s
E	=	total energy per unit mass, J/kg
f	=	frequency, 1/s
H	=	total enthalpy per unit mass, J/kg
h	=	enthalpy per unit mass, J/kg
h_k	=	enthalpy per unit mass for species k, J/kg
H_j^{sgs}	=	subgrid-scale total enthalpy flux vector, J/(m^2 · s)
h^{sgs}	=	subgrid-scale species mass fraction-enthalpy correlation, J/kg
J	=	jet-to-crossflow momentum flux ratio
k	=	turbulent kinetic energy, m^2/s^2
k^{sgs}	=	subgrid-scale kinetic energy, m^2/s^2
M	=	Mach number
m	=	mass flow rate, kg/s
M_w	=	molecular weight, kg/mol
p	=	static pressure, Pa
Pr_t	=	turbulent Prandtl number
p_t	=	total pressure, Pa
q_j	=	heat flux vector, J/(m^2 · s)
q_j^{sgs}	=	subgrid-scale energy diffusion due to species diffusion, J/(m^2 · s)
R	=	mixture's gas constant, J/(kg · K)
R_k	=	gas constant for species k, J/(kg · K)
Re_D	=	Reynolds number based on D
r_s	=	spatial correlation coefficient
r_{ts}	=	time–space correlation coefficient
S_{ij}	=	rate of strain tensor, 1/s
Sc_t	=	turbulent Schmidt number
T	=	static temperature, K
t	=	time, s
T_t	=	total temperature, K
T^{sgs}	=	subgrid-scale mixture gas constant-temperature correlation, J/kg
T^0	=	reference temperature, K
U	=	velocity magnitude, m/s
u, v, w	=	velocity components in x, y, and z directions, m/s
U_c	=	convection velocity, m/s
u_i	=	velocity component in x_i direction, m/s
$V_{j,k}$	=	species diffusion velocity vector for species k, m/s
x, y, z	=	streamwise, transverse, and spanwise direction distances in Cartesian coordinates, m
x_i	=	Cartesian coordinates, m
Y_k	=	mass fraction for species k
$Y_{j,k}^{\text{sgs}}$	=	subgrid-scale species diffusion vector, kg/(m^2 · s)
γ	=	specific heat ratio
$\Delta h_{f,k}^0$	=	standard heat of formation at T^0, J/kg
δ_{in}	=	mean boundary-layer thickness at inlet, m
η_m	=	mixing efficiency
$\theta_{j,k}^{\text{sgs}}$	=	subgrid-scale species mass fraction-diffusion velocity correlation, kg/(m^2 · s)
κ	=	mixture's thermal conductivity, J/(m · K · s)
μ	=	mixture's molecular viscosity, kg/(m · s)
ν_t	=	subgrid-scale eddy viscosity, m^2/s
ρ	=	density, kg/m^3
σ_{ij}	=	viscous stress tensor, Pa
σ_j^{sgs}	=	subgrid-scale viscous work, J/(m^2 · s)
τ_{ij}^{sgs}	=	subgrid-scale stress tensor, Pa
φ	=	local equivalence ratio

Subscripts

j	=	injection condition or injectant
rms	=	root mean square
∞	=	crossflow

Superscripts

$\bar{}$	=	spatial filter
$\tilde{}$	=	Favre filter

Presented as Paper 2011-5764 at the 47th AIAA/ASME/SAE/ASEE Joint Propulsion Conference and Exhibit, San Diego, CA, August 1–3, 2011; received 30 August 2011; revision received 8 November 2011; accepted for publication 9 November 2011.

*Ph.D. Student, Department of Aerospace Engineering. Student Member AIAA.
†Assistant Professor, Department of Aerospace Engineering. Member AIAA.
‡Associate Professor, Department of Aerospace Engineering. Member AIAA.
§Professor, Department of Aerospace Engineering. Senior Member AIAA.

$\bar{\ }$ = time average
$''$ = fluctuation from time average

I. Introduction

SUPERSONIC combustors have been studied and developed in many countries as a potential hypersonic propulsion device. Inside a supersonic combustor, rapid mixing between the injected fuel and incoming supersonic airflow is essential because the flow residence time is short. The fuel mixing in the supersonic airflow is dominated by turbulent motion, and so a detailed understanding of the turbulent mixing mechanism is important for developing successful fuel mixing inside a supersonic combustor. Many researchers have experimentally [1–3] or numerically [4–6] investigated the flowfield of an air jet injected into a supersonic crossflow, revealing many turbulent features. However, these features may not be the same as those for an injected fuel jet. Hydrogen is a promising candidate fuel for supersonic combustors because its heat of reaction per unit mass and burning velocity are high. However, hydrogen's low density requires a large storage tank. On the other hand, hydrocarbon fuels are attractive because of their higher density and consequent ease of storage. The large difference of molecular weight associated with these fuels leads to a wide variation in properties such as the injection velocity and density. In addition, the fuels' compressibility levels are believed to be different, and most likely cause different turbulent behaviors in jet-crossflow mixing. In some past experiments, differences of turbulent structure for injectant species with different molecular weights have been observed. Gruber et al. [7] compared planar Rayleigh/Mie scattering images for helium and air jets transversely injected into Mach 2 crossflow. They estimated the convective Mach number M_c for each injectant gas and investigated the effects of compressibility on the development of a large-scale turbulent structure. Takahashi et al. [8] also investigated the large-scale turbulent structure of helium and air jets transversely injected into Mach 2 and 2.5 crossflows using acetone planar laser-induced fluorescence (PLIF) measurement. Figure 1 shows representative PLIF images for helium and air jets. The large-scale turbulent structure that appears in the windward side of the jet plume can be clearly seen. The large-scale structures seem to be somewhat different for helium and air jets. Takahashi et al. characterized the shape and size of large-scale turbulent structures in the scalar field by using a single-time two-point spatial correlation analysis. Also, Ben-Yakar et al. [9] visualized the time evolution of hydrogen and ethylene transverse jets by using high-speed schlieren imaging. They tracked the large-scale structure and obtained its convection velocity and growth rate for each fuel. The ethylene jet had a slower convection velocity and larger growth rate than the hydrogen jet. However, the turbulent behavior has not been well determined, quantitatively and in detail, owing to the difficulty of making direct and precise measurements in a supersonic flowfield and the complicated three-dimensional features of the jet in a supersonic crossflow configuration. As a result, numerical investigation might be an effective tool for improving our understanding. In particular, with the recent advancement of computational resources, large-eddy simulation (LES) is becoming a powerful and attractive method for the analysis of supersonic turbulent flow.

We performed LESs of transverse jets in a Mach 1.9 crossflow to investigate the differences in the turbulent behavior associated with injectant species. Hydrogen, helium, nitrogen, and ethylene jets were simulated. In this study, we mainly focused on the large-scale structure that develops in the windward mixing layer between the transverse jet and supersonic crossflow. This structure plays an important role in the large-scale mixing (entrainment of the crossflow air into the jet plume) in the near field [6]. The comparison between the different injectant gases was made at a constant jet-to-crossflow momentum flux ratio J because it is well known that the jet penetration in the averaged field is governed by J [1,10,11]. Instantaneous features of the jets for each injectant gas were investigated first. Greater differences in the instantaneous velocity fields for different injectants were revealed. Then, the time-averaged field was compared. The LES time-series data were analyzed by using statistical approaches, such as turbulent intensity analysis, spectral analysis, and probability density function (PDF) evaluation. These analyses provided new findings on the different turbulent features for different injectants. Also, the convection characteristics of the windward large-scale structure were statistically evaluated by using the two-time two-point scalar correlation, and they were compared between the injectants. Also, the mixing state was compared between the hydrogen and ethylene jets. The preset study revealed the significantly different turbulent mixing properties between, depending on the fuel species.

II. Numerical Methods

A. Governing Equations and Subgrid-Scale Model

The governing equations are the spatially filtered mass, momentum, total energy, species conservation equations, and the perfect gas equation of state:

$$\frac{\partial \bar{\rho}}{\partial t} + \frac{\partial \bar{\rho}\tilde{u}_j}{\partial x_j} = 0 \tag{1}$$

$$\frac{\partial \bar{\rho}\tilde{u}_j}{\partial t} + \frac{\partial}{\partial x_j}(\bar{\rho}\tilde{u}_i\tilde{u}_j + \bar{p}\delta_{ij} - \tilde{\sigma}_{ij} + \tau_{ij}^{\text{sgs}}) = 0 \tag{2}$$

$$\frac{\partial \bar{\rho}\tilde{E}}{\partial t} + \frac{\partial}{\partial x_j}[(\bar{\rho}\tilde{E} + \bar{p})\tilde{u}_j + \hat{q}_j - \tilde{\sigma}_{ij}\tilde{u}_i + H_j^{\text{sgs}} + \sigma_j^{\text{sgs}} + q_j^{\text{sgs}}] = 0 \tag{3}$$

$$\frac{\partial \bar{\rho}\tilde{Y}_k}{\partial t} + \frac{\partial}{\partial x_j}(\bar{\rho}\tilde{Y}_k\tilde{u}_j + \bar{\rho}\tilde{Y}_k\tilde{V}_{j,k} + Y_{j,k}^{\text{sgs}} + \theta_{j,k}^{\text{sgs}}) = 0 \tag{4}$$

$$\bar{p} = \bar{\rho}(\tilde{R}\tilde{T} + T^{\text{sgs}}) \tag{5}$$

Here, the Favre filtered form of the total energy per unit mass is defined by

$$\tilde{E} = \tilde{h} - \frac{\bar{p}}{\bar{\rho}} + \frac{1}{2}\tilde{u}_i\tilde{u}_i + k^{\text{sgs}} \tag{6}$$

For calorically perfect gases, the filtered enthalpy is given by

$$\tilde{h} = \sum_k \tilde{h}_k\tilde{Y}_k + h^{\text{sgs}} = (\tilde{T} - T^0)\sum_k c_{p,k}\tilde{Y}_k + \sum_k \Delta h_{f,k}^0\tilde{Y}_k + h^{\text{sgs}} \tag{7}$$

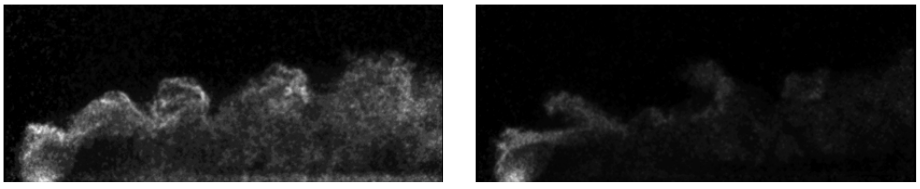

a) He jet **b) Air jet**

Fig. 1 Representative acetone PLIF images.

The value of $c_{p,k}$ is constant and taken as that for temperature T^0. The filtered form of R is obtained as

$$\tilde{R} = \sum_k R_k \tilde{Y}_k \tag{8}$$

The terms $\tilde{\sigma}_{ij}$, $\hat{q}_j$, and $\tilde{V}_{j,k}$ are given by

$$\tilde{\sigma}_{ij} = 2\mu(\tilde{S}_{ij} - \tfrac{1}{3}\tilde{S}_{kk}\delta_{ij}) \tag{9}$$

$$\hat{q}_j = -\kappa \frac{\partial \tilde{T}}{\partial x_j} - \bar{\rho} \sum_k \tilde{h}_k D_k \frac{\partial \tilde{Y}_k}{\partial x_j} \tag{10}$$

$$\tilde{V}_{j,k} = -\frac{D_k}{\tilde{Y}_k} \frac{\partial \tilde{Y}_k}{\partial x_j} \tag{11}$$

The transport coefficients for each species are calculated by using a fourth-order polynomial fit at the filtered temperature. The mixture's transport coefficients are obtained using Wilke's formulation [12].

The subgrid-scale (SGS) terms need to be modeled to close the equations. The SGS stress τ_{ij}^{sgs} is closed by using the eddy viscosity model as

$$\tau_{ij}^{\text{sgs}} = -2\bar{\rho}\nu_t(\tilde{S}_{ij} - \tfrac{1}{3}\tilde{S}_{kk}\delta_{ij}) + \tfrac{2}{3}\bar{\rho}k^{\text{sgs}}\delta_{ij} \tag{12}$$

The selective mixed-scale model [13] is used to evaluate the SGS eddy viscosity. The detailed modeling of ν_t and the SGS kinetic energy k^{sgs} is described in [13]. The SGS total enthalpy flux H_j^{sgs} is calculated from the gradient diffusion model by using ν_t [14]:

$$H_j^{\text{sgs}} = -\bar{\rho}\frac{\nu_t}{Pr_t}\frac{\partial \tilde{H}}{\partial x_j} \tag{13}$$

where the filtered total enthalpy is defined as $\tilde{H} = \tilde{h} + (1/2)(\tilde{u}_i\tilde{u}_i) + k^{\text{sgs}}$, and Pr_t is assumed to be $Pr_t = 0.9$. The SGS species diffusions $Y_{j,k}^{\text{sgs}}$ in the gradient diffusion model are

$$Y_{j,k}^{\text{sgs}} = -\bar{\rho}\frac{\nu_t}{Sc_t}\frac{\partial \tilde{Y}_k}{\partial x_j} \tag{14}$$

where Sc_t is taken to be $Sc_t = 0.9$. The SGS viscous work σ_j^{sgs}, the SGS energy diffusion due to species diffusion q_j^{sgs}, the SGS species mass fraction-diffusion velocity correlation $\theta_{j,k}^{\text{sgs}}$, the SGS mixture gas constant-temperature correlation T^{sgs}, and the SGS species mass fraction-enthalpy correlation h^{sgs} are neglected here.

B. Numerical Schemes

The equations described in the previous section are solved in generalized curvilinear coordinates. The convection fluxes are evaluated by using the AUSM-family upwind scheme named SLAU [15] with the fourth-order MUSCL approach [16]. The diffusion fluxes are computed by using the second-order central differential scheme. The time advancement is performed with the third-order classical Runge–Kutta scheme. The computational time step is fixed throughout the calculation, and the maximum inviscid Courant–Friedrichs–Lewy (CFL) number is about 0.5 for all cases. The LES with the aforementioned schemes and the SGS models were validated by comparison with experiments for compressible mixing layers [17] and a transverse air jet into a supersonic crossflow [6].

C. Computational Grid and Configuration

In this study, LES is applied to a transverse jet injected into a supersonic crossflow from a circular hole on a flat plate. Figure 2 shows the computational grid used in this study. The injector hole is located at the bottom boundary, and its diameter is $D = 2.5$ mm. The center of the injector hole lies $18D$ downstream of the inlet on the centerline of the bottom boundary. The origin of the Cartesian coordinate system (x, y, z) is taken to be at the center of the injector hole. The crossflow direction (streamwise direction) is x, the wall-normal direction is y, and the spanwise direction is z. The region framed by broken lines in Fig. 2 is the main domain, which is $26D$ long, $8D$ high, and $8D$ wide. The buffer regions, where the mesh spacing coarsens toward the boundaries, are placed outside the main domain to damp turbulent fluctuations and suppress unphysical reflections of the fluctuations at the boundaries [5]. The flowfield in the buffer regions will not be discussed. The grid is structured and consists of hexahedral cells. The number of grid points in the main domain is $293 \times 181 \times 153$ $(x \times y \times z)$. The grid is clustered near the injector in the x direction and near the bottom boundary in the y direction. The grid stretching factor is less than 1.09 in each direction. The minimum and maximum mesh spacings in the x and y directions are $\Delta x_{\min}/D \sim 0.05$, $\Delta x_{\max}/D \sim 0.1$, $\Delta y_{\min}/D \sim 0.003$, and $\Delta y_{\max}/D \sim 0.05$ in the main domain. The mesh spacing is constant in the z direction in the main domain ($\Delta z/D \sim 0.05$). The present grid resolution is finer than that of the fine grid used in our previous LES for a transverse air jet in a supersonic crossflow [6] by a factor of 1.2. In [6], the error bound due to insufficient grid resolution was estimated to be 10–15% for the injectant mass fraction distributions from the grid sensitivity study. Therefore, we note that the possible error bound in the present LES would be within 10–15%.

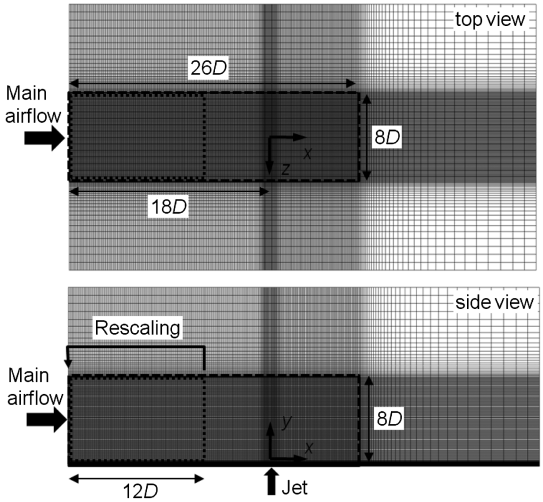

Fig. 2 Side and top views of the computational grid.

D. Boundary Conditions

The flow conditions are basically chosen to enable a comparison of the LES results with experimental data from Takahashi et al. [8]. The crossflow Mach number is $M_\infty = 1.9$, the total pressure is $p_{t\infty} = 100$ kPa, and the total temperature is $T_{t\infty} = 290$ K at the inlet boundary. The crossflow Reynolds number based on the injector diameter is $Re_D = 3.3 \times 10^4$. In the wall injection, the state of the incoming boundary layer has a large impact on jet mixing [5]. To reproduce the incoming turbulent boundary layer, the rescaling method [18,19] modified by Sagaut et al. [20] is applied in the $12D$ length domain that is framed by dotted lines in Fig. 2. The mean boundary-layer thickness at the inlet is fixed at $\delta_{\text{in}} = 2.5$ mm.

In the present LES, four kinds of injectant gases are simulated and compared with each other: hydrogen, helium, nitrogen, and ethylene. All gases are injected perpendicular to the crossflow at sonic speed. The total temperature of injectant gas is $T_{tj} = 290$ K for all gases. Table 1 summarizes the injection conditions simulated. For the comparison between the injectant gases, the jet-to-crossflow momentum flux ratio is fixed at $J = 1.9$. The injectant molecular weight $M_{w,j}$; the injectant specific heat ratio γ_j; the jet-to-crossflow velocity, density, and pressure ratios U_j/U_∞, ρ_j/ρ_∞, and p_j/p_∞, respectively; and the jet mass flow rate m_j are also listed in the table.

Table 1 Summary of injection conditions ($D = 2.5$ mm, $M_j = 1.0$)

Injectant gas	J	$M_{w,j}$, g/mol	γ_j	U_j/U_∞	ρ_j/ρ_∞	p_j/p_∞	m_j, g/s
Hydrogen (H_2)	1.9	2	1.40	2.39	0.33	6.88	0.62
Helium (He)	1.9	4	1.67	1.75	0.62	5.78	0.84
Nitrogen (N_2)	1.9	28	1.40	0.64	4.63	6.88	2.29
Ethylene (C_2H_4)	1.9	28	1.23	0.62	4.90	7.81	2.36

The upstream flowfield in the injector pipe may affect the flowfield in the computational domain, especially near the injector. However, this effect will not be significant for the comparison of turbulent behaviors of different injectant species, because turbulent behavior is primarily affected by the interaction between the transverse jet and the crossflow. Therefore, we did not simulate the upstream injector pipe to reduce the computational cost. Instead, the injection condition is uniformly imposed at all grid points within a distance of $D/2$ from the center of the injector on the bottom boundary, and the injection condition is fixed throughout the calculation. Note that the turbulent flowfield developing inside the injector pipe is neglected because of these simplified injection conditions.

The bottom boundary, except for the injection port, is assumed to be a no-slip and adiabatic wall. At the top, side, and outlet boundaries, where the buffer regions exist, the computation simply extrapolates the variables from the interior points.

III. Results and Discussion

In the following, we use the nondimensional time, $t^* = t \cdot U_\infty/D$, which is normalized by the diameter of the injector hole D and the undisturbed crossflow velocity U_∞. The computational time step is $\Delta t^* \sim 4 \times 10^{-4}$ for the hydrogen and helium injection cases, and $\Delta t^* \sim 1 \times 10^{-3}$ for the nitrogen and ethylene injection cases. Injectant gases with smaller molecular weights require smaller Δt^* because the CFL number is larger due to the faster sonic speed. The following statistical data were obtained from the LES results using 800 time-series data points at intervals of $\Delta t^* = 0.5$ (corresponding to a physical sampling rate of 400 kHz), which were sampled after the time-averaged flowfield had converged sufficiently. In this time interval, the undisturbed crossflow covers a distance of $0.5D$. Therefore, the unsteady time-sequence behavior is captured well enough at this sampling rate. For the spectral analysis, the data were sampled at intervals of $\Delta t^* = 0.02$ to capture the high-frequency turbulence.

A. Comparisons with Experiments

First, we compare the LES results with the available acetone PLIF data [8]. In the PLIF measurement, acetone vapor was seeded in the injectant gas (air or helium). The LIF signal under the present conditions is believed to be linearly proportional to the molar concentration of the injectant gas [21]. Therefore, in this study, we compare the averaged distribution of the injectant molar concentration, the rms distribution, and the spatial correlation distribution of the injectant molar concentration fluctuation obtained from the LES result with the acetone PLIF image. In the acetone PLIF, 500 time-independent data points are processed to obtain the statistical data. In previous work [6], we have compared LES results with acetone PLIF data for an air jet in a supersonic crossflow. We obtained good agreement, especially for the windward jet structure. We compare the results for the helium jet here.

Figure 3 shows the comparison of the averaged distributions of injectant molar concentration in the centerplane ($z/D = 0$) for a helium jet. The concentration distribution in the LES is normalized by the value at the injector exit. The LIF signal is also normalized, but the reference value for the normalization is the space-averaged value in the region a little bit above the injector exit where the jet fluid expands. Moreover, the LIF signal near the injector exit is probably contaminated by light scattered by the wall. In Fig. 3b, we can observe a high-intensity band due to this scattered light (around $y/D = 0.2$). For these reasons, the normalized concentration in the acetone PLIF is believed to be shifted to larger values than those in the LES over the whole region. Therefore, a quantitative comparison is difficult. But, qualitatively, the overall patterns of the distributions are similar: for example, the shape of barrel shock wave and the position of the Mach disk are almost the same. In the figures, the maximum averaged concentration track at each x/D location (solid line) and the averaged concentration tracks for 50 and 10% of the maximum value on the windward side (broken and dashed–dotted lines) are also drawn. Quantitative comparison of these tracks is possible because they are not affected by the concentration shift in the acetone PLIF associated with the normalization. The maximum track in LES lies at almost the same position as that in the PLIF, though it is slightly lower at $x/D > 7$. The 50 and 10% tracks in LES lie slightly higher than those in the PLIF, but the trajectory shapes are similar. Thus, reasonable agreement was obtained for the averaged injectant concentration field.

Figure 4 shows the comparison of the rms distributions of the injectant molar concentration fluctuation in the centerplane for the LES and the acetone PLIF in the helium injection case. The maximum-, 50%-, and 10%-averaged concentration tracks are also drawn in the figure. Overall, a similar distribution to that of the PLIF is obtained for the LES. An intensively fluctuating region appears in the windward mixing layer between the jet and the crossflow. The most intensively fluctuating region lies along the 50%-averaged concentration track. Also, a region of high rms values appears along the windward part of the barrel shock wave. These features are captured well by our LES.

The features of the turbulent structure on the windward side of the jet plume are compared next. Takahashi et al. [3,8] used the single-time two-point spatial correlation coefficient r_s for the geometrical characterization of the large-scale structure:

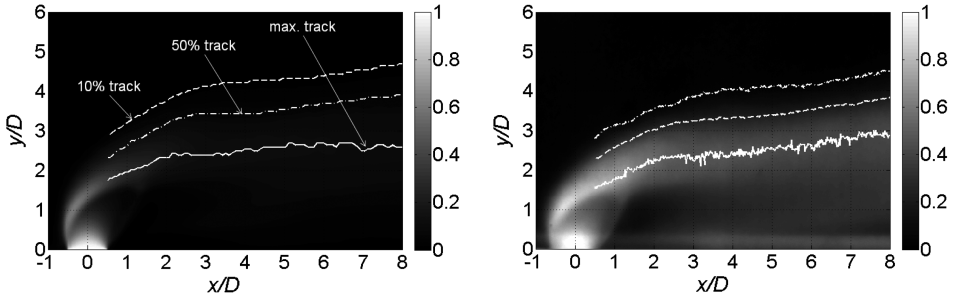

a) LES **b) Acetone PLIF**

Fig. 3 Comparison of averaged injectant molar concentration distributions in the centerplane (He jet).

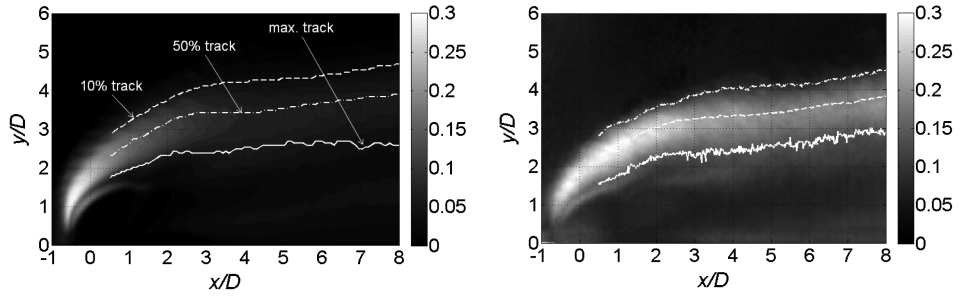

a) LES **b) Acetone PLIF**

Fig. 4 Comparison of rms injectant molar concentration fluctuation distributions in the centerplane (He jet).

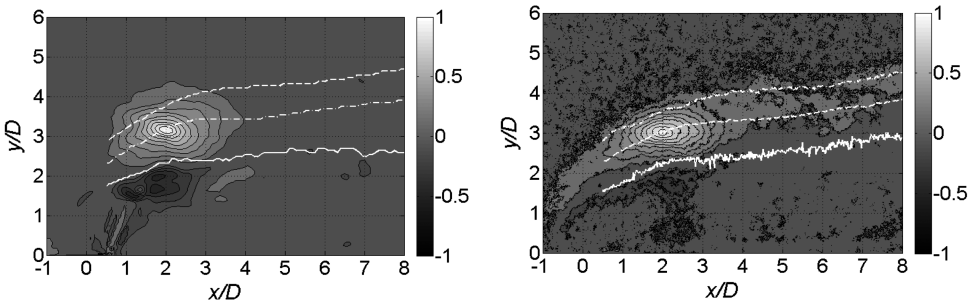

a) LES **b) Acetone PLIF**

Fig. 5 Comparison of two-point spatial correlations of injectant molar concentration fluctuations in the centerplane.

$$r_s(\Delta x, \Delta y) = \frac{(1/N)\sum_{i=1}^{N}[C''_{j,i}(x,y)\cdot C''_{j,i}(x+\Delta x, y+\Delta y)]}{C''_{j,\mathrm{rms}}(x,y)\cdot C''_{j,\mathrm{rms}}(x+\Delta x, y+\Delta y)} \tag{15}$$

Here, point (x, y) is the reference location with which the features are correlated; Δx and Δy are the spatial differences in the x and y directions, respectively; and N is the number of data used. Figure 5 shows the comparison of the single-time two-point spatial correlation map based on the injectant molar concentration fluctuation in the helium injection case. The reference point is at $x/D = 2$ on the 50%-averaged concentration track. If the concentration shift in the acetone PLIF data is the same throughout, a quantitative comparison of r_s maps would be possible because the effect of concentration shift would be canceled out, owing to the normalization by $C''_{j,\mathrm{rms}}$ in Eq. (15). The highly positive correlation region, which represents the large-scale structure, lies around the reference point and has an elliptical shape. The major axis of the ellipse is almost parallel to the x direction in both correlation maps. In the PLIF map, a weak positive correlation region with an elongated shape appears across the windward mixing layer. On the other hand, such a region does not appear in the LES map. However, the value of the correlation coefficient in the elongated region is below $r_s = 0.2$, which is not of considerable value. A negatively correlated region appears below the maximum averaged concentration track in both correlation maps, though the magnitude of the correlation coefficient is not large. This region may be caused by jet flapping. To compare the shape of the windward large-scale structure at specific streamwise stations, the $r_s = 0.5$ contours for reference points on the 50%-averaged concentration track at $x/D = 2, 4, 6$, and 8 are illustrated in Fig. 6. Although differences between the LES and the PLIF exist, the overall shape and size of the $r_s = 0.5$ contour is captured by our LES. Overall, our LES can reproduce the windward large-scale structure for the helium jet to a reasonable extent.

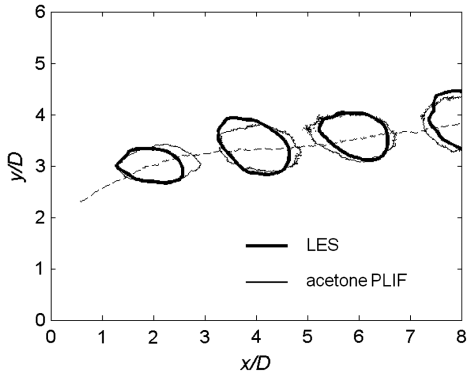

Fig. 6 Comparison between LES (bold lines) and acetone PLIF (thin lines) of streamwise change of $r_s = 0.5$ contour in the centerplane.

B. Instantaneous Structure

In the previous section, we discussed the jet structure by using the injectant molar concentration for the comparison with the acetone PLIF data. However, the molar concentration is affected by the local density. The effect of the local density is strong, especially near the injector, because a large density gradient exists there. In contrast, the injectant mole or mass fraction is not affected by the local change of density and, therefore, is proper for the observation of the jet structure.

Figure 7 shows instantaneous distributions of the injectant mass fraction for each injectant gas in the centerplane. Three representative instantaneous distributions are shown. For the distributions of hydrogen and ethylene jets, the stoichiometric lines are also drawn as bold lines. Prominent large-scale structures on the windward side of the jet plume are indicated by arrows in each figure. The overall instantaneous jet structure is similar for the hydrogen and helium jets. In the hydrogen and helium jets, the prominent windward large-scale structures are elongated in the streamwise direction, although the identity of the structures is somewhat unclear. The jet structures of the nitrogen and ethylene jets are also similar but have different features from those of hydrogen and helium jets. The large-scale structures are more noticeable than for the hydrogen and helium jets. These structures protrude into the supersonic crossflow and incline toward the upstream and upward directions. These protrusions have a characteristic counterclockwise rotating structure. Between these protrusions, the braid region, where the crossflow air intrudes deep into the jet core, is prominent. These aforementioned

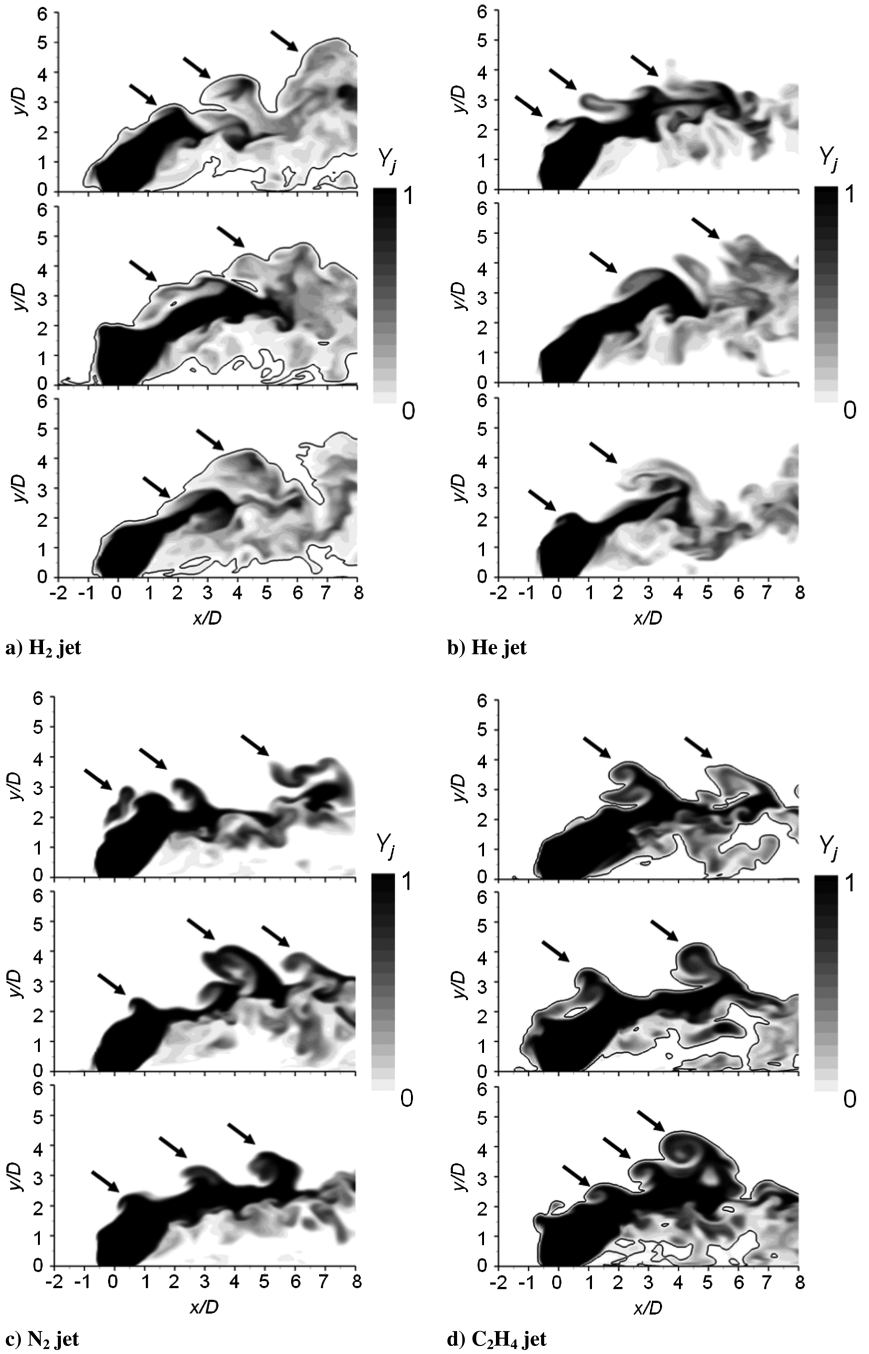

Fig. 7 Instantaneous injectant mass fraction distributions in the centerplane.

observations are similar to those in the previous observations using Rayleigh/Mie scattering by Gruber et al. [7], in which the helium and air injections were compared.

Figure 8 shows instantaneous distributions of the velocity vectors in the centerplane for each injectant gas. The length of the vector represents the magnitude of the velocity. In the cases of hydrogen and helium jets, the velocity magnitude in the jet plume is much larger than that in the crossflow. Therefore, a high strain rate exists between the jet and the crossflow for these jets. The large-scale structure could be strongly stretched in the streamwise direction by this large velocity gradient; thus, the elongated structure observed in Figs. 7a and 7b is formed. On the other hand, the velocity difference between the jet and the crossflow is small for the nitrogen and ethylene jets. The difference of the velocity field contributes to the difference of the large-scale structure.

Next, the features of the jet structure in the cross-sectional plane are investigated. Figure 9 shows instantaneous distributions of the injectant mass fraction for each injectant gas in the $x/D = 4$ cross-sectional plane. Three representative instantaneous distributions are shown. The stoichiometric lines are drawn in the distributions of the hydrogen and ethylene jets. For all injectant gases, the jet structure varies greatly in time and has a highly three-dimensional shape. Axisymmetric jet protrusions do not exist. Comparing these distributions for the different injectant gases, we see that the instantaneous jet structure for nitrogen and ethylene has a thin shape with some elongated protrusions and its shape is highly variable. On the other hand, the jet structure in the hydrogen and helium jets seems to be broad compared to the nitrogen and ethylene jets. This is because the region around the jet core region (black) in which the jet is mixed with the crossflow air (gray) is wider than it is for the nitrogen and ethylene jets. The geometric variability of the hydrogen and helium jet structures seems to be less than that of the nitrogen or ethylene jet. This implies the existence of some highly intermittent feature in the nitrogen and ethylene jets.

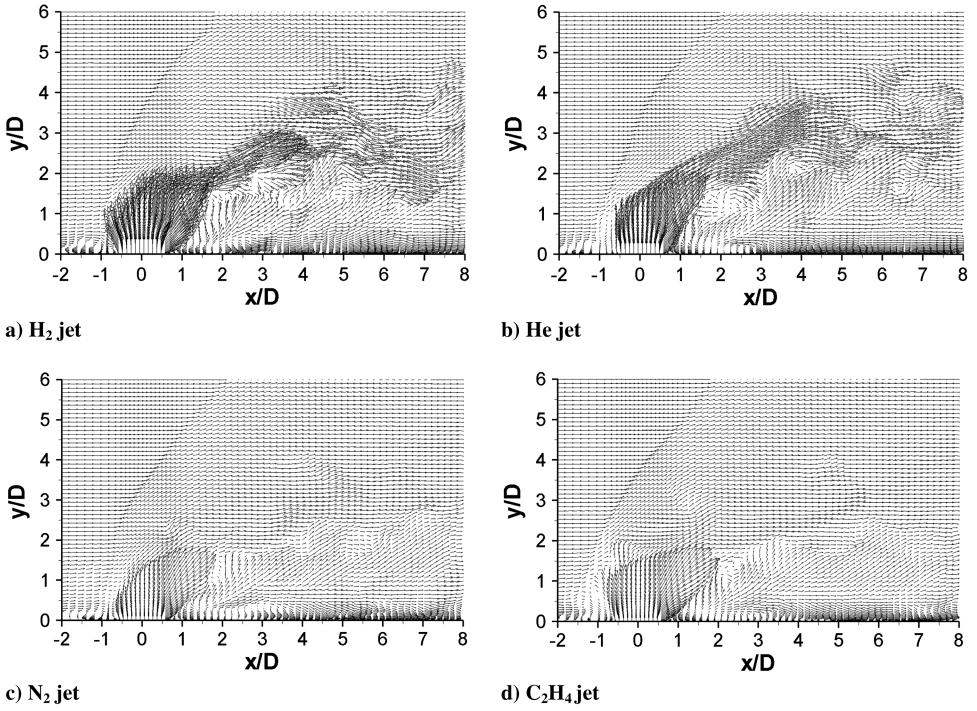

Fig. 8 Instantaneous velocity vector distributions in the centerplane.

C. Time-Averaged Field

Figure 10 shows the time-averaged distributions of injectant mass fraction in the centerplane for each injectant gas. The averaged maximum, 50%, and 10% injectant mass fraction tracks on the windward side are also shown as broken lines. The shape of the barrel shock wave depends on the injectant species. The spatial extent of barrel shock structure is large for the ethylene jet and is small for the helium jet. The shape of the barrel shock wave depends on the specific heat ratio of the injectant γ_j. For all injectant gases, the unmixed jet core in the averaged field disappears at around $x/D = 3$, but the unmixed jet core remains much further downstream in the instantaneous field, as shown in Fig. 7. To examine the penetration height, the averaged injectant mass fraction tracks are compared in Fig. 11. The averaged injectant mass fraction tracks are roughly consistent with each other. In particular, the 10% tracks for all injectants are well consistent with each other. The maximum and 50% tracks of nitrogen and ethylene jets are slightly lower than those of hydrogen and helium jets downstream of $x/D = 2$. As a result, the gaps between the maximum and 10% tracks in hydrogen and helium jets are slightly narrower than those of nitrogen and ethylene jets. This trend agrees qualitatively with observations based on acetone PLIF measurements [8] in which the helium and air jets are compared. However, these differences in the maximum and 50% tracks for different injectants may not be significant because of the uncertainties due to the statistical convergence and the finite grid resolution. Therefore, we conclude that the jet penetration defined by the averaged injectant mass fraction field is almost the same irrespective of the injectant species when the jet-to-crossflow

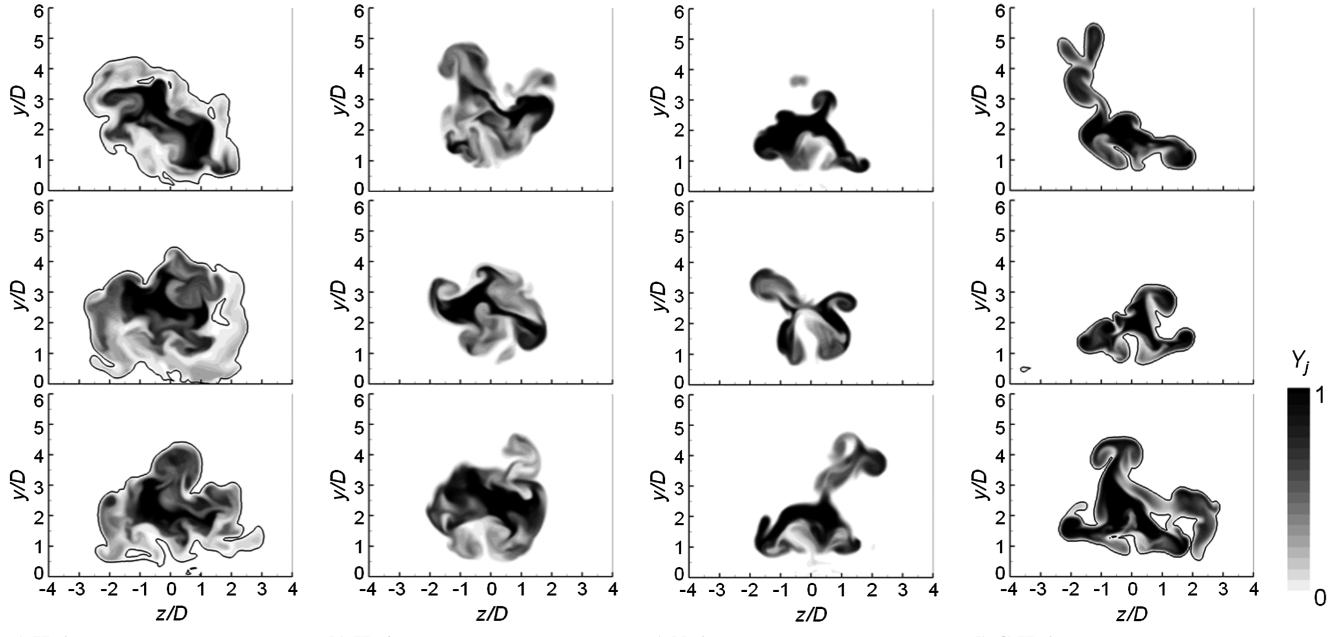

Fig. 9 Instantaneous injectant mass fraction distributions in the $x/D = 4$ cross-sectional plane.

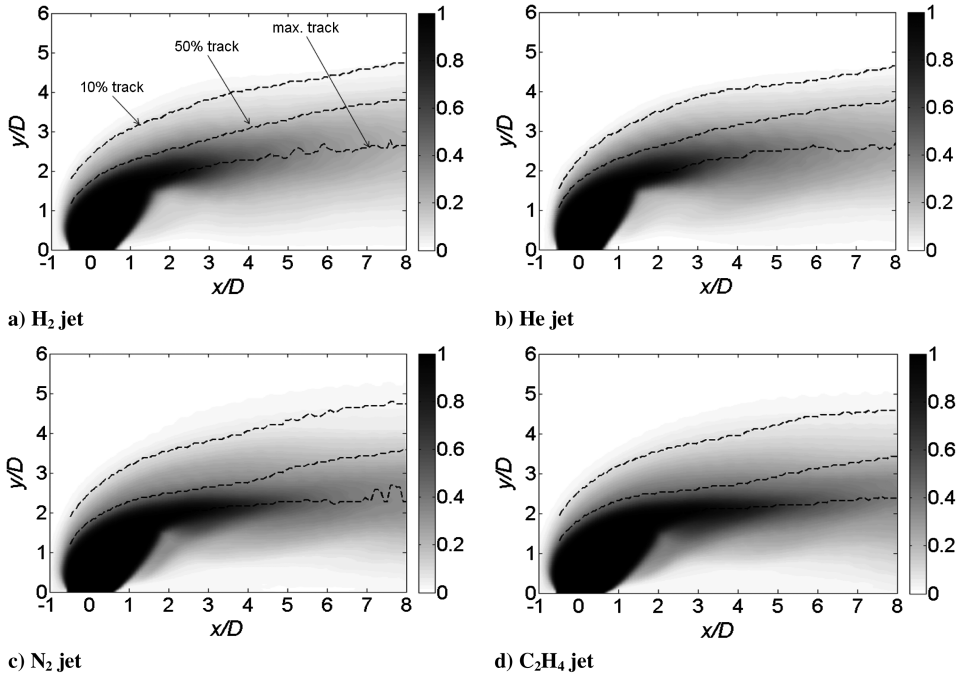

a) H_2 jet b) He jet

c) N_2 jet d) C_2H_4 jet

Fig. 10 Time-averaged injectant mass fraction distributions in the centerplane.

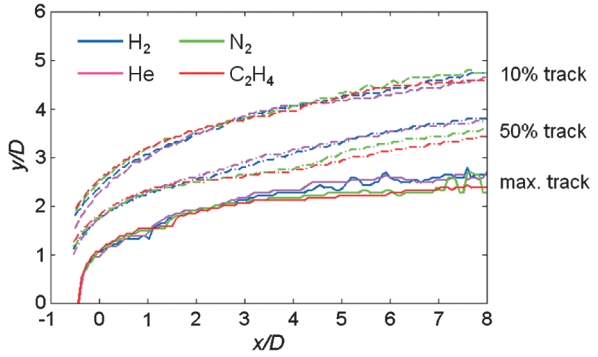

Fig. 11 Comparison of maximum-, 50%-, and 10%-averaged injectant mass fraction tracks.

momentum flux ratio is the same. This result is consistent with the experiment of Gruber et al. [7].

Figure 12 shows the time-averaged distributions of velocity magnitude for each injectant gas in the centerplane. The velocity magnitude is normalized by U_∞. The averaged injectant mass fraction tracks are also drawn in the figure to provide an understanding of the relation between the velocity field and the injectant concentration field. In the hydrogen and helium jets, a region with a much faster velocity than that of the crossflow exists in the jet plume. Interestingly, the maximum injectant mass fraction track (solid line) does not lie over the maximum velocity track. The maximum velocity tracks in the hydrogen and helium jets lie above the maximum injectant mass fraction tracks. On the other hand, in the nitrogen and ethylene jets, a region with slightly slower velocity than that of the crossflow exists downstream of the Mach disk, and a

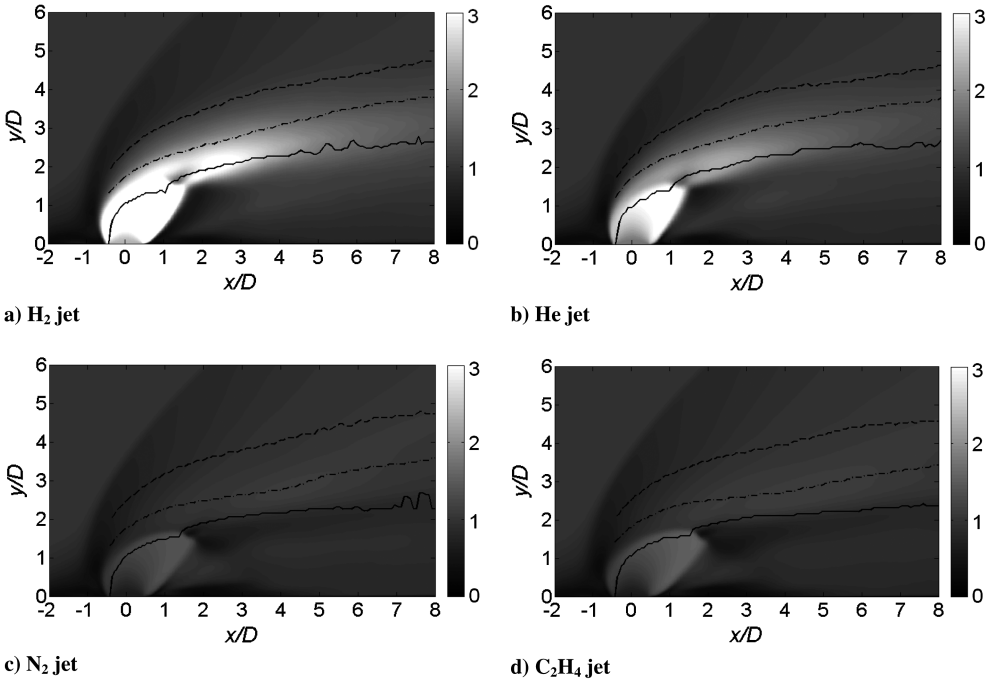

a) H_2 jet b) He jet

c) N_2 jet d) C_2H_4 jet

Fig. 12 Time-averaged velocity magnitude distributions in the centerplane.

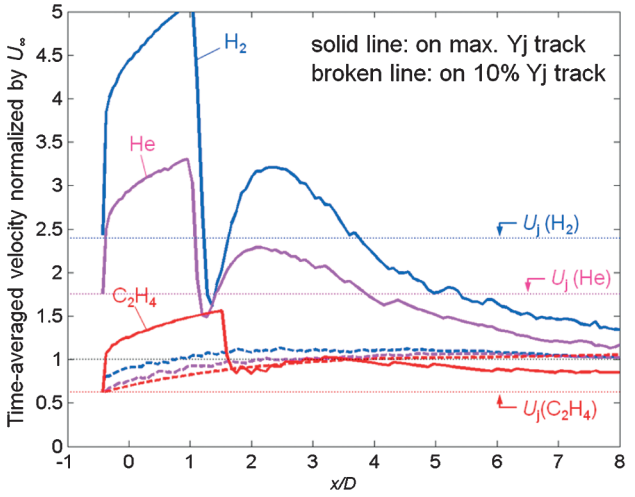

Fig. 13 Time-averaged velocity magnitude on maximum- and 10%-averaged mass fraction tracks.

waketype flow is formed behind the jet. The minimum velocity tracks in the wake lie below the maximum injectant mass fraction tracks.

Figure 13 shows the time-averaged velocity magnitudes, normalized by U_∞, on the maximum and 10% injectant mass fraction tracks for hydrogen, helium, and ethylene jets. The result of nitrogen jet is omitted in order to make the figure clear. The nitrogen result is almost identical to the ethylene result. The injection velocity of each injectant gas is also shown by a dotted line. The velocity difference between these tracks is likely to be one of the most important factors influencing the turbulent structure developing in the windward mixing layer. The velocity on the 10% injectant mass fraction track (broken line) is roughly the same for all the injectant gases and is approximately equal to U_∞. In contrast, the velocity on the maximum injectant mass fraction track (solid line) is different for each injectant gas. For all injectant gases, the velocity increase due to the initial expansion of the underexpanded jet and the rapid velocity decrease at the Mach disk are observed. Downstream of the Mach disk, the hydrogen and helium jets accelerate again, and then the velocity gradually decreases downstream of $x/D = 2$. On the other hand, the velocities of the nitrogen and ethylene jets are almost constant, at a velocity slightly below U_∞. The velocity difference between the jet and the crossflow is considerable in the near field for the hydrogen and helium jets. However, the velocity difference is smaller downstream; the velocity difference of helium jet is the same as that of nitrogen and ethylene jets at $x/D = 8$.

D. Turbulent Features of Velocity Field

Figure 14 shows the turbulent kinetic energy (TKE) distributions in the centerplane for each injectant species. The TKE is defined by $k = (1/2) \cdot (\bar{\tilde{u}}''^2 + \bar{\tilde{v}}''^2 + \bar{\tilde{w}}''^2)$. The TKE is normalized by $(\Delta U)^2$, where $\Delta U = |U_j - U_\infty|$. For all injectant species, high TKE regions exist along the edge of the barrel shock wave, indicating the fluctuation of the barrel shock wave. In the nitrogen and ethylene jets, a high TKE region exists behind the barrel shock wave, where a waketype flow is formed, as shown in Fig. 12. The TKE for nitrogen and ethylene is not so large in the windward mixing layer. In the hydrogen and helium jets, a high TKE region extends from the downstream edge of the Mach disk, which corresponds to the leeward boundary of the jet. Moreover, an additional high TKE region exists in the windward mixing layer, in contrast to the nitrogen and ethylene jets. A large velocity difference between the jet and the crossflow exists in this region for the hydrogen and helium jets, as shown in Figs. 8, 12, and 13. It should be noted that the real TKE level (without normalization) is much higher for the hydrogen and helium jets than for the nitrogen and ethylene jets, although the normalized TKE levels in the nitrogen and ethylene jets are higher (ΔU is 688 m/s for the H_2 jet, 372 m/s for the He jet, 178 m/s for the N_2 jet, and 188 m/s for the C_2H_4 jet). Also, we confirmed that the real TKE in the separation region upstream of the jet and in the near-wall region downstream was the same for all injectant species.

Figure 15 shows the power spectrum of the streamwise velocity fluctuation u'' normalized by ΔU at $(x/D, y/D, z/D) = (4, 2.8, 0)$ for hydrogen, helium, and ethylene jets. The nitrogen result is omitted because it is almost identical to the ethylene result. This position is near the 50% averaged injectant mass fraction track in the windward mixing layer. To obtain the spectra, the data were sampled at intervals of $\Delta t^* = 0.02$ (corresponding to a physical sampling rate of 10 MHz). The horizontal axis is the frequency f normalized by D and ΔU. A line with a $-\frac{5}{3}$ slope is also shown in the figure. For all

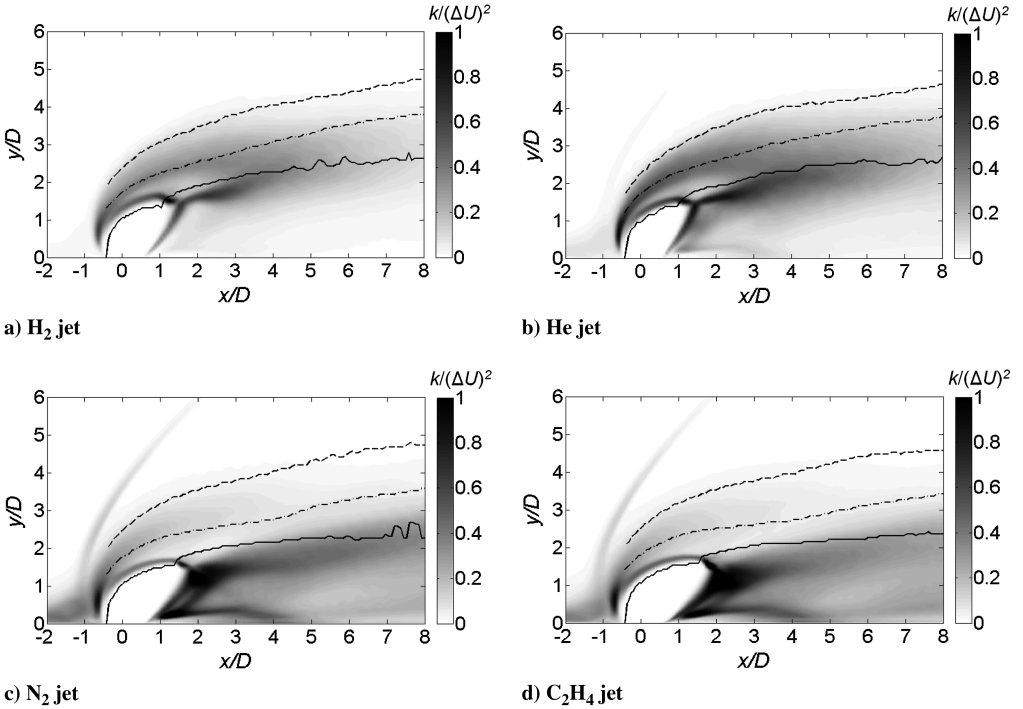

Fig. 14 TKE distributions in the centerplane.

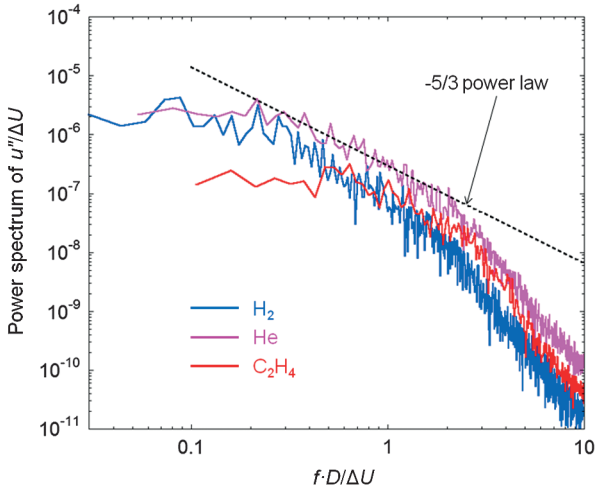

Fig. 15 Power spectra of streamwise velocity fluctuations at $(x/D, y/D, z/D) = (4, 2.8, 0)$.

injectant species, the region in which the spectrum follows Kolmogorov's $-\frac{5}{3}$ power law exists; that is, our LES resolves at least a part of the inertial subrange. For cases of normalization by D and ΔU, the spectra for injectant species match to a reasonable extent in the high-frequency range. Only in the low-frequency range do the spectra have different distributions. The spectra of the hydrogen and helium jets have longer inertial subranges than those of the nitrogen and ethylene jets. Larger-scale energetic eddies are contained in the windward mixing layer for the hydrogen and helium jets, and the turbulent energy is transferred to smaller-scale eddies by the energy cascade following Kolmogorov's law. Also, a distinct peak cannot be observed in the spectra for any of the injectant species. Therefore, the periodicity of the windward structure is not strong.

E. Probability Density Functions

We now analyze the PDFs of the injectant mass fraction at representative stations to discuss quantitatively the intermittency of jets observed in the instantaneous distributions. Figures 16 and 17 show the PDFs at $x/D = 4$ and 8 in the centerplane ($z/D = 0$) for each injectant gas. The horizontal axis represents the injectant mass fraction, and the vertical axis represents the transverse location y/D. The probability value is indicated by the color contour. The time average and the standard deviation profiles of injectant mass fraction are also indicated by a black solid line and a red broken line, respectively.

First, we note some common characteristics of the PDFs at $x/D = 4$ (Fig. 16). At large y/D locations, the PDF peak near $Y_j = 0$ indicates mostly unmixed crossflow fluid. As y/D decreases, the probability near $Y_j = 0$ gradually decreases and the probability of intermediate Y_j values, which indicates a mixed fluid, increases. Around the jet core (the peak of mean Y_j), a high PDF peak appears near $Y_j = 1$. At the same time, a PDF peak near $Y_j = 0$ still remains above the jet core; the PDF is bimodal. This shows the intermittent appearance of the unmixed jet and the unmixed crossflow in the windward mixing layer. At the jet core, the PDF peak near $Y_j = 0$ disappears. Below the jet core, the high PDF peak near $Y_j = 1$ disappears and a high PDF peak near $Y_j = 0$ appears again as y/D decreases. In the leeward mixing layer, relatively high probability regions in the intermediate range of Y_j occur around the mean Y_j profile: that is, the PDF is closer to a Gaussian profile in the leeward mixing layer than it is in the windward mixing layer. This indicates the steadiness of the mixing state in the leeward mixing layer compared to the windward mixing layer. These trends are consistent with the observations in the PDF for an air jet obtained by the acetone PLIF signals [2,22]. They also discussed the intermittent nature in the windward mixing layer and the relatively steady mixing state in the leeward mixing layer.

Next, we note the differences of PDF features at $x/D = 4$. The overall PDF distributions are very similar for hydrogen and helium, and for nitrogen and ethylene. This trend is consistent with the instantaneous distributions shown in Figs. 7 and 9. However, markedly different features can be observed in the windward mixing layer. In the PDF distributions of hydrogen and helium, a high probability region exists in the relatively low range of $Y_j < 0.4$. This region is near the mean Y_j profile. On the other hand, the PDFs of nitrogen and ethylene in the windward mixing layer are highly bimodal compared to those of hydrogen and helium. In addition, the PDFs of nitrogen and ethylene cover the whole intermediate range of Y_j without a prominent peak. A weak peak exists near $Y_j = 0.6$, but this peak departs from the mean Y_j profile. These PDF features strongly indicate the high intermittency of nitrogen and ethylene jets in the windward mixing layer.

Further downstream, at $x/D = 8$ (Fig. 17), the mixing has progressed for all injectant species. The PDFs of hydrogen and helium are Gaussian-like even in the windward mixing layer. The unmixed jet ($Y_j = 1$) no longer exists for the hydrogen and helium jets at $x/D = 8$. On the other hand, in the nitrogen and ethylene jets, a small probability for an unmixed jet still remains, and the PDF covers a wider Y_j range. The highly intermittent features of the nitrogen and ethylene jets still remain at $x/D = 8$.

F. Convection Characteristics of the Windward Large-Scale Structure

The convection of the windward large-scale structure is evaluated by using the time–space correlation of the injectant mass fraction fluctuation in the centerplane. The two-time two-point correlation of the injectant mass fraction fluctuation in the centerplane is defined by

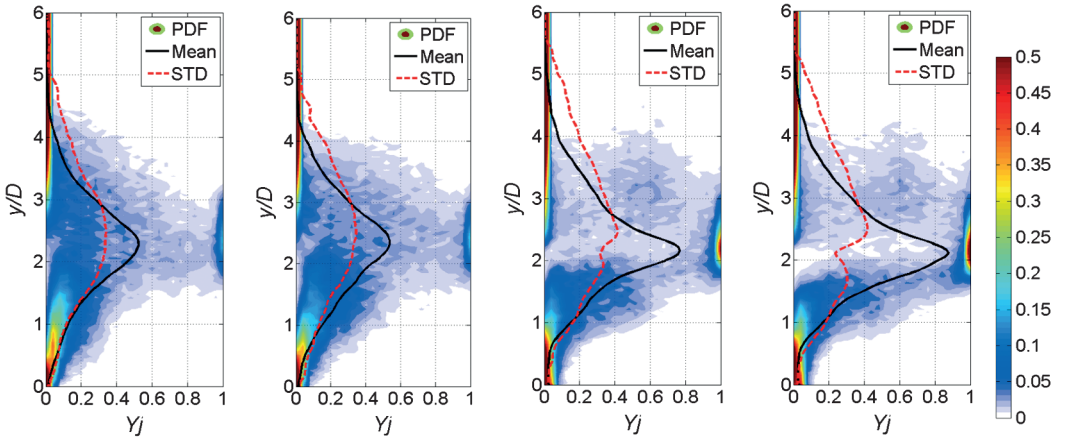

a) H_2 jet **b) He jet** **c) N_2 jet** **d) C_2H_4 jet**

Fig. 16 PDFs of injectant mass fraction at $x/D = 4$ in the centerplane. Mean: time-average profile; STD: standard deviation profile.

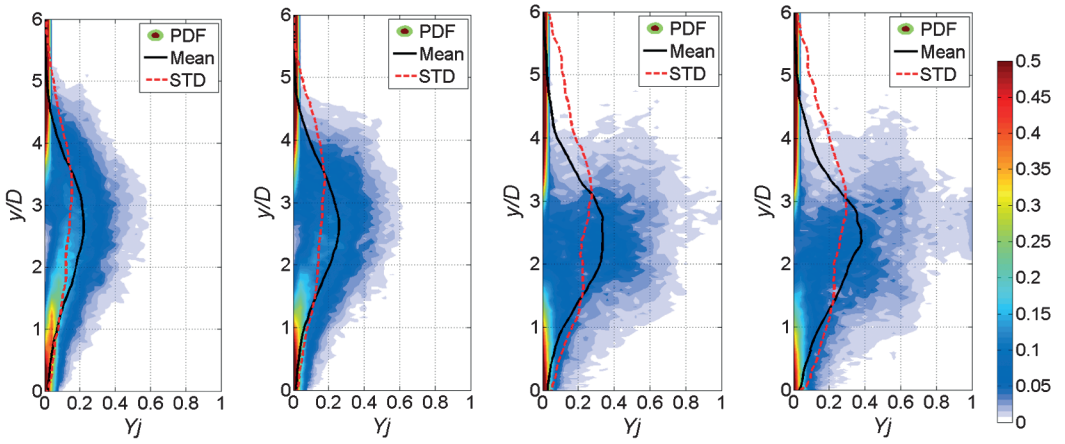

a) H_2 jet b) He jet c) N_2 jet d) C_2H_4 jet

Fig. 17 PDFs of injectant mass fraction at $x/D = 8$ in the centerplane. Mean: time-average profile; STD: standard deviation profile.

$$r_{ts}(\Delta x, \Delta y, \Delta t) = \frac{(1/N)\sum_{i=1}^{N}[Y''_{j,i}(x, y, t) \cdot Y''_{j,i}(x + \Delta x, y + \Delta y, t + \Delta t)]}{Y''_{j,\mathrm{rms}}(x, y) \cdot Y''_{j,\mathrm{rms}}(x + \Delta x, y + \Delta y)} \tag{16}$$

where Δt is the temporal difference. For $\Delta t = 0$, the time–space correlation r_{ts} reduces to the spatial correlation r_s. In the present analysis, Δt is fixed at $\Delta t^* = 0.5$, and Δx and Δy are varied over the entire range in the domain to obtain the correlation map in the centerplane. From the correlation map, the maximum correlation point $(x_{\max}, y_{\max})$ is found. The displacement from (x, y) to $(x_{\max}, y_{\max})$ is taken to be the convection of the large-scale structure during Δt. Then, the point $(x_{\max}, y_{\max})$ is taken as the new reference point (x, y), and the correlation map is calculated again. By repeating this procedure, we can track the convection of the large-scale structure. The initial reference point is set at $x/D = 0.5$ on the maximum track of the rms distribution for the injectant mass fraction fluctuation. The convection velocity of the large-scale structure U_c can be calculated as

$$U_c = \frac{\sqrt{(x_{\max} - x)^2 + (y_{\max} - y)^2}}{\Delta t} \tag{17}$$

Another method of calculating the trajectory of the large-scale structure is to fix the reference point at its initial location and change Δt. Then, the positively correlated region moved downstream and the maximum value of r_{ts} decreased as Δt increased. When Δt was large, a distinct maximum correlation point did not exist and a weak positive correlation region was evenly spread over a wide range. In such cases, the trajectory of the maximum correlation point scattered and the convection velocity had a large error. Therefore, we do not show the results of this procedure here.

Figure 18 shows the tracks of the large-scale structure for each injectant species. The maximum correlation points are plotted as open circles. The tracks for each injectant species are not notably different from each other and are near to the 50%-averaged injectant mass fraction track. The contours of $r_{ts} = 0.5$, which is taken as representing the shape and size of the large-scale structure, are also depicted by bold lines for every second tracking point. Near the injector, an elongated shape along the track is prominent in the contours for hydrogen and helium, showing that the large-scale structure is stretched by the large velocity difference there (see Fig. 13). In the downstream region, a tilted elliptical shape is visible for all injectant species. The size of the $r_{ts} = 0.5$ contour is large for the hydrogen jet and small for the nitrogen jet. The critical factor determining the size of the large-scale structure is still unclear. A possible factor is the velocity difference between the jet and the crossflow: a larger velocity difference would produce a larger-scale structure. However, the different sizes of the structures for the nitrogen and ethylene jets cannot be explained in this way because there is little velocity difference between the nitrogen and ethylene jets. A more detailed understanding requires further study.

The convection velocity of the large-scale structure estimated from Eq. (17) is shown in Fig. 19. The nitrogen result is omitted in the figure because it is almost identical to the ethylene result. The horizontal axis is the streamwise position, and the vertical axis is the convection velocity normalized by U_∞. The error bar is set so that the maximum correlation point can change within a ± 0.5 grid spacing in the x and y directions. The injection velocity U_j for each injectant gas is shown as a reference. For the ethylene (and nitrogen), the convection velocity is slower than U_j upstream of the barrel shock wave ($x/D < 0$). As the jet bends downstream, the convection velocity gradually increases and reaches U_∞ at around $x/D = 2$. Further downstream, it is almost constant at U_∞. On the other hand, the convection velocity for hydrogen and helium shows a somewhat different trend from that of ethylene. Even though the injection velocity of hydrogen and helium is much faster than U_∞, the convection velocity near the injector is lower than U_∞. This might be because the crossflow is strongly decelerated there by passing through the bow shock wave, as shown in Fig. 12. As the jet bends downstream, the convection velocity rapidly increases and reaches about $U_c/U_\infty = 1.5$, but it does not reach the injection velocity U_j. The convection velocity of hydrogen is faster than that of helium. However, this difference is not as large as the difference between the injection velocities. Downstream of $x/D = 5$, the convection velocity gradually decreases and may converge on the crossflow velocity further downstream. The convection velocity for each injectant gas is almost within the range between the time-averaged velocities on the maximum and 10%-averaged mass fraction tracks shown in Fig. 13. The downstream convection velocities show little difference among the injectant species. Therefore, the compressibility levels would not be notably different, although the hydrogen and helium jets would suffer higher compressibility effects than the nitrogen and ethylene jets in the near field.

G. Mixing Efficiency

In this section, we evaluate the mixing efficiency for the hydrogen and ethylene jets. The mixing efficiency evaluation is based on both instantaneous and time-averaged quantities. The mixing efficiency based on the instantaneous quantities is given by

$$\eta_{m,\mathrm{inst}} = \frac{\iint(\tilde{\rho}\,\tilde{u}\,\tilde{Y}_j/\tilde{\varphi}')\,\mathrm{d}y\,\mathrm{d}z}{m_j} \qquad \tilde{\varphi}' = \begin{cases} 1 & (\tilde{\varphi} \le 1) \\ \tilde{\varphi} & (\tilde{\varphi} > 1) \end{cases} \tag{18}$$

On the other hand, the mixing efficiency based on the time-averaged quantities is given by

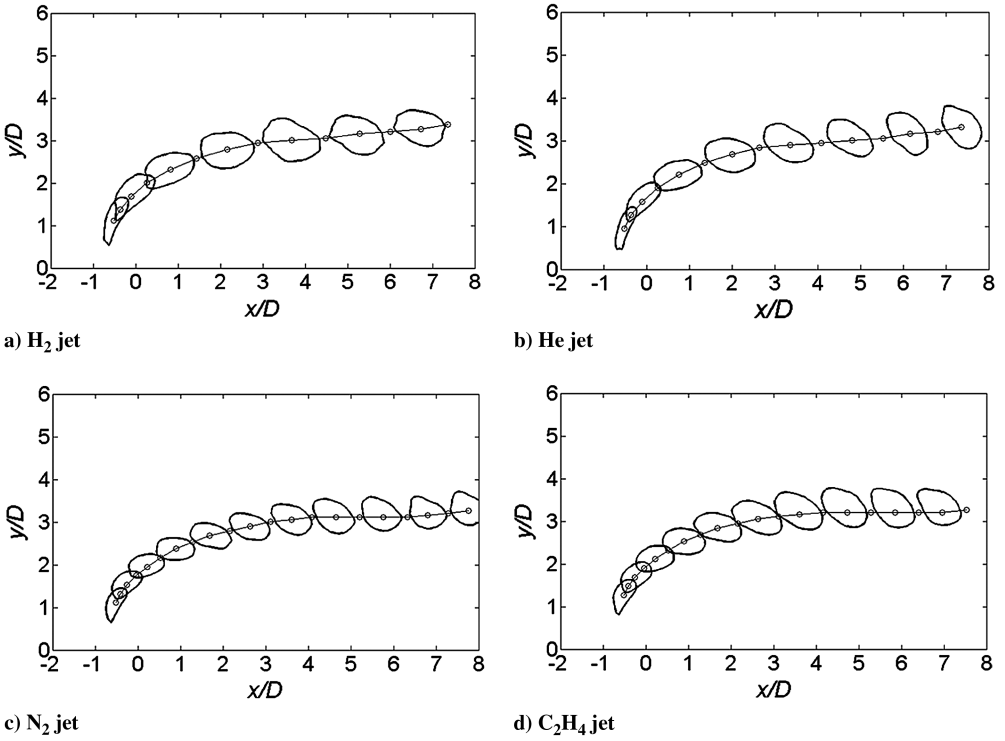

Fig. 18 Tracks of windward large-scale structure with $r_{ts} = 0.5$ contours.

$$\eta_{m,\mathrm{ave}} = \frac{\iint (\bar{\tilde{\rho}}\,\bar{\tilde{u}}\,\bar{\tilde{Y}}_j/\bar{\tilde{\varphi}}')\,\mathrm{d}y\,\mathrm{d}z}{m_j} \qquad \bar{\tilde{\varphi}}' = \begin{cases} 1 & (\bar{\tilde{\varphi}} \le 1) \\ \bar{\tilde{\varphi}} & (\bar{\tilde{\varphi}} > 1) \end{cases} \tag{19}$$

The instantaneous evaluation is desirable because the combustion state depends on the instantaneous mixing state. However, the mixing evaluation has often been conducted by using time- or ensemble-averaged data, such as probe measurements and computational fluid dynamics based on the Reynolds-averaged Navier–Stokes (RANS) equations. The comparison of instantaneous and averaged mixing efficiencies was conducted in the hybrid RANS/LES simulation of Peterson and Candler [23], and they revealed the large difference between those two mixing efficiencies for the ethylene jet. Here, we compare these mixing efficiencies for the hydrogen and ethylene jets.

Figure 20 shows the instantaneous and time-averaged mixing efficiencies for the hydrogen and ethylene jets. The instantaneous mixing efficiency is evaluated at $x/D = 1, 2, 3, 4, 5, 6, 7$, and 8. The average of 800 instantaneous mixing efficiencies at intervals of $\Delta t^* = 0.5$ is plotted as an open circle, and the standard deviation of its fluctuation is shown as an error bar. The mixing efficiency based on the time-averaged quantities is shown as a solid line. The mixing efficiency of ethylene is larger than that of hydrogen in the time-averaged evaluation, but this is reversed in the instantaneous evaluation. The average of the instantaneous mixing efficiency is about half that of the mixing efficiency based on the time-averaged quantities for the hydrogen jet. On the other hand, the average instantaneous mixing efficiency is below one-third that of the time-averaged efficiency in the ethylene jet. The large discrepancy between the instantaneous and time-averaged mixing efficiencies in the ethylene jet is caused by the highly intermittent behavior, which is revealed by the PDFs shown in Figs. 16 and 17. The instantaneous mixing efficiency of the hydrogen jet is much larger than that of the ethylene jet; at $x/D = 8$, the instantaneous mixing efficiency of the hydrogen jet is twice as large as that of the ethylene jet. The better mixing in the hydrogen jet most likely results from the higher TKE. As discussed in Sec. III.D (Fig. 14), a much higher TKE was obtained for the hydrogen jet than in the ethylene jet due to the larger difference between the injection and crossflow velocities ΔU. In the windward mixing layer of the hydrogen jet, a lot of crossflow air is entrained by larger-scale energetic eddies containing small-scale eddies (see Fig. 15). Thus, enhanced mixing would occur for the hydrogen jet. It should be noted that this trend may change under real scramjet combustor conditions in which the crossflow velocity is

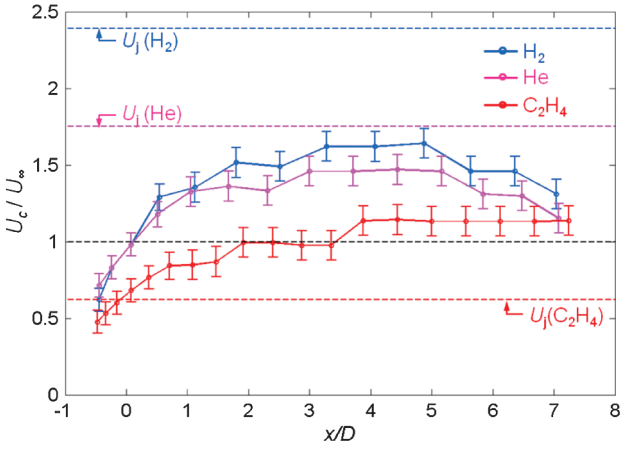

Fig. 19 Convection velocity of windward large-scale structure.

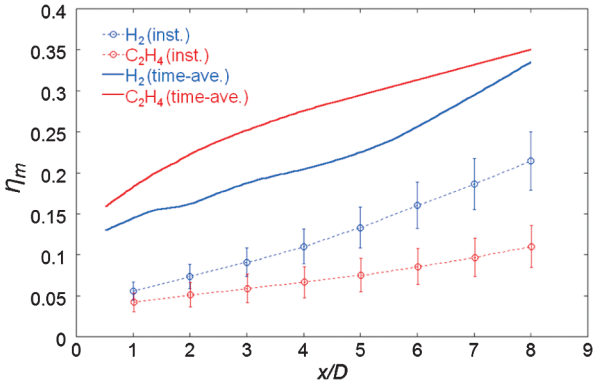

Fig. 20 Instantaneous (inst.) and time-averaged (time-ave.) mixing efficiencies for hydrogen and ethylene jets.

much faster than the present cold flow condition due to the higher static temperature of crossflow air. In such a case, the large velocity difference would exist for the ethylene jet rather than for the hydrogen jet, because the ethylene jet is much slower than the crossflow. Therefore, a higher TKE may be obtained for an ethylene jet, leading to greater mixing efficiency. We think that the velocity difference between the jet and the crossflow is the most important factor controlling the turbulent properties and the mixing state, as also pointed out by Ben-Yakar et al. [9].

IV. Conclusions

Large-eddy simulations (LESs) of underexpanded transverse jets of various injectant species (hydrogen, helium, nitrogen, and ethylene) injected into Mach 1.9 supersonic crossflow were conducted to investigate the effect of injectant species on the turbulent structure and mixing of the jet. The comparison was conducted at a fixed jet-to-crossflow momentum flux ratio condition ($J = 1.9$). First, the LES results were compared with acetone planar laser-induced fluorescence data for a helium jet. The characteristic features of the averaged and root-mean-square distributions of injectant molar concentration were qualitatively reproduced by our LES. In addition, the size and shape of the large-scale structure appearing on the windward side of the jet plume were compared by using the single-time two-point scalar spatial correlation, and reasonable agreement was obtained. The following conclusions were reached concerning the effects of injectant species on jet turbulent mixing:

1) The features of windward large-scale jet protrusions were significantly different between injectant gases with smaller molecular weight and faster injection velocity (hydrogen and helium) and injectant gases with larger molecular weight and slower injection velocity (nitrogen and ethylene), although highly three-dimensional jet protrusions were observed in all injectant gases. The nitrogen and ethylene jets had more noticeable large-scale structures inclining toward the upstream and upward directions. On the other hand, in the hydrogen and helium jets, the large-scale structure was strongly elongated in the streamwise direction. The unsteady geometric change of the jet plume was more intensive in the nitrogen and ethylene jets. These were consistent with the observations by experimental visualizations.

2) The jet penetration defined by the time-averaged injectant mass fraction distribution was almost the same, irrespective of the injectant species when the jet-to-crossflow momentum flux ratio was the same. This trend agreed with the previous observations.

3) Large differences were observed in the velocity field, corresponding to differences in injection velocity. In the near field, a very large velocity difference between the jet and the crossflow existed in the hydrogen and helium jets. However, as the jet flowed parallel to the crossflow downstream, the velocity difference rapidly decreased.

4) Due to the large velocity difference between the jet and the crossflow, a much higher TKE developed in the hydrogen jet. For the nitrogen and ethylene jets, a high TKE region existed in the wake behind the jet plume. For the hydrogen and helium jets, high TKE regions developed in the windward mixing layer and downstream of the Mach disk.

5) Spectral analysis revealed that larger-scale energetic eddies were formed in the windward mixing layer for the hydrogen and helium jets, and the turbulent energy transferred well to small-scale eddies, even in the near field at $x/D = 4$.

6) The PDFs of the injectant mass fraction were strongly bimodal in the windward mixing layer for the nitrogen and ethylene jets. This indicates a high intermittency for nitrogen and ethylene jets.

7) The convection characteristics were evaluated by using the time–space correlation of injectant mass fraction fluctuations. The convection velocity of hydrogen and helium jets was much larger than that of nitrogen and ethylene in the near field. However, the convection velocity approached the crossflow velocity downstream for all injectant gases. The convection characteristics were different only in the near field.

8) A greater difference between the mixing efficiency based on time-averaged quantities and that based on instantaneous quantities existed in the ethylene jet compared with the hydrogen jet. This is due to ethylene's highly intermittent behavior. The mixing efficiency of the hydrogen jet based on instantaneous quantities was about twice as high as that of the ethylene jet. This would be due to the higher TKE in the mixing layer of the hydrogen jet and to the existence of larger energetic eddies accompanying the energy cascade to small eddies in the windward mixing layer for the hydrogen jet.

Acknowledgments

This work was supported by a Grant-in-Aid for the Japan Society for the Promotion of Science Fellows, number 21·4309. The authors are grateful to H. Takahashi, who provided the experimental data. Numerical simulation was conducted using supercomputing resources at the Cyberscience Center at Tohoku University.

References

[1] Gruber, M. R., Nejad, A. S., Chen, T. H., and Dutton, J. C., "Mixing and Penetration Studies of Sonic Jets in a Mach 2 Freestream," *Journal of Propulsion and Power*, Vol. 11, No. 2, March 1995, pp. 315–323. doi:10.2514/3.51427

[2] VanLerberghe, W. M., Santiago, J. G., Dutton, J. C., and Lucht, R. P., "Mixing of a Sonic Transverse Jet Injected into a Supersonic Flow," *AIAA Journal*, Vol. 38, No. 3, March 2000, pp. 470–479. doi:10.2514/2.984

[3] Takahashi, H., Oso, H., Kouchi, T., Masuya, G., and Hirota, M., "Scalar Spatial Correlation in a Supersonic Mixing Flowfield," *AIAA Journal*, Vol. 48, No. 2, Feb. 2010, pp. 443–452. doi:10.2514/1.44684

[4] Peterson, D. M., and Candler, G. V., "Hybrid Reynolds-Averaged and Large-Eddy Simulation of Normal Injection into a Supersonic Crossflow," *Journal of Propulsion and Power*, Vol. 26, No. 3, May–June 2010, pp. 533–544. doi:10.2514/1.46810

[5] Kawai, S., and Lele, S. K., "Large-Eddy Simulation of Jet Mixing in Supersonic Crossflow," *AIAA Journal*, Vol. 48, No. 9, Sept. 2010, pp. 2063–2083. doi:10.2514/1.J050282

[6] Watanabe, J., Kouchi, T., Takita, K., and Masuya, G., "Numerical Study on the Turbulent Structure of Transverse Jet into Supersonic Flow," *AIAA Journal*, Vol. 49, No. 9, Sept. 2011, pp. 2057–2067. doi:10.2514/1.J051067

[7] Gruber, M. R., Nejad, A. S., Chen, T. H., and Dutton, J. C., "Compressibility Effects in Supersonic Transverse Injection Flowfield," *Physics of Fluids*, Vol. 9, No. 5, May 1997, pp. 1448–1461. doi:10.1063/1.869257

[8] Takahashi, H., Masuya, G., and Hirota, M., "Effects of Injection and Main Flow Conditions on Supersonic Turbulent Mixing Structure," *AIAA Journal*, Vol. 48, No. 8, Aug. 2010, pp. 1748–1756. doi:10.2514/1.J050355

[9] Ben-Yakar, A., Mungal, M. G., and Hanson, R. K., "Time Evolution and Mixing Characteristics of Hydrogen and Ethylene Jets in Supersonic Crossflows," *Physics of Fluids*, Vol. 18, 2006, Paper 026101. doi:10.1063/1.2139684

[10] Smith, S. H., and Mungal, M. G., "Mixing, Structure and Scaling of the Jet in Crossflow," *Journal of Fluid Mechanics*, Vol. 357, 1998, pp. 83–122. doi:10.1017/S0022112097007891

[11] Papamoschou, D., and Hubbard, D. G., "Visual Observations of Supersonic Transverse Jets," *Experiments in Fluids*, Vol. 14, 1993, pp. 468–476. doi:10.1007/BF00190201

[12] Wilke, C. R., "A Viscosity Equation for Gas Mixtures," *Journal of Chemical Physics*, Vol. 18, No. 4, 1950, pp. 517–519. doi:10.1063/1.1747673

[13] Lenormand, E., Sagaut, P., and Ta Phuoc, L., "Large Eddy Simulation of Subsonic and Supersonic Channel Flow at Moderate Reynolds Number," *International Journal for Numerical Methods in Fluids*, Vol. 32, Feb. 2000, pp. 369–406. doi:10.1002/(SICI)1097-0363(20000229)32:4<369::AID-FLD943>3.0.CO;2-6

[14] Menon, S., and Patel, N., "Subgrid Modeling for Simulation of Spray Combustion in Large-Scale Combustor," *AIAA Journal*, Vol. 44, No. 4, April 2006, pp. 709–723.

doi:10.2514/1.14875
[15] Shima, E., and Kitamura, K., "On New Simple Low-Dissipation Scheme of AUSM-Family for All Speeds," AIAA Paper 2009-0136, 2009.
[16] Yamamoto, S., and Daiguji, H., "Higher-Order-Accurate Upwind Schemes for Solving the Compressible Euler and Navier–Stokes Equations," *Computers and Fluids*, Vol. 22, No. 2, March–May 1993, pp. 259–270.
doi:10.1016/0045-7930(93)90058-H
[17] Watanabe, J., Kouchi, T., Takita, K., and Masuya, G., "Large-Eddy Simulation of Compressible Mixing Layers," *Proceedings of the Seventh International Conference on Flow Dynamics*, Tohoku Univ., Sendai, Japan, 2010, pp. 540–541.
[18] Spalart, P. R., "Direct Simulation of a Turbulent Boundary Layer up to $R_\theta = 1410$," *Journal of Fluid Mechanics*, Vol. 187, 1988, pp. 61–98.
doi:10.1017/S0022112088000345
[19] Lund, T. S., Wu, X., and Squires, K. D., "Generation of Turbulent Inflow Data for Spatially-Developing Boundary Layer Simulations," *Journal of Computational Physics*, Vol. 140, 1998, pp. 233–258.
doi:10.1006/jcph.1998.5882
[20] Sagaut, P., Garnier, E., Tromeur, E., Larcheveque, L., and Labourasse, E., "Turbulent Inflow Conditions for Large-Eddy Simulation of Compressible Wall-Bounded Flows," *AIAA Journal*, Vol. 42, No. 3, March 2004, pp. 469–477.
doi:10.2514/1.3461
[21] Takahashi, H., Ikegami, S., Oso, H., Masuya, G., and Hirota, M., "Quantitative Imaging of Injectant Mole Fraction and Density in Supersonic Mixing," *AIAA Journal*, Vol. 46, No. 11, Nov. 2008, pp. 2935–2943.
doi:10.2514/1.37783
[22] Takahashi, H., "Experimental Study of Scalar Structure in a Supersonic Turbulent Mixing Flowfield Using Acetone PLIF," Ph.D. Dissertation, Aerospace Engineering Dept., Tohoku Univ., Sendai, Japan, March 2003.
[23] Peterson, D. M., and Candler, G. V., "Supersonic Combustor Fuel Injection Simulations Using a Hybrid RANS/LES Approach," AIAA Paper 2010-0411, 2010.

P. Tucker
Associate Editor